

Beyond Geo-localization: Fine-grained Orientation of Street-view Images by Cross-view Matching with Satellite Imagery

Wenmiao Hu
Grab-NUS AI Lab, NUS
hu.wenmiao@u.nus.edu

Yichen Zhang
Grab-NUS AI Lab, NUS
zhang.yichen@u.nus.edu

Yuxuan Liang
National University of Singapore
yuxliang@outlook.com

Yifang Yin
Institute for Infocomm Research,
A*STAR
yin_yifang@i2r.a-star.edu.sg

Andrei Georgescu
Grab Chronos S.R.L.
andrei.georgescu@grabtaxi.com

An Tran
Grabtaxi Holdings Pte. Ltd.
an.tran@grabtaxi.com

Hannes Kruppa
Grabtaxi Holdings Pte. Ltd.
hannes.kruppa@grabtaxi.com

See-Kiong Ng
Grab-NUS AI Lab, NUS
seekiong@nus.edu.sg

Roger Zimmermann
Grab-NUS AI Lab, NUS
rogerz@comp.nus.edu.sg

ABSTRACT

Street-view imagery provides us with novel experiences to explore different places remotely. Carefully calibrated street-view images (e.g., Google Street View) can be used for different downstream tasks, e.g., navigation, map features extraction. As personal high-quality cameras have become much more affordable and portable, an enormous amount of crowdsourced street-view images are uploaded to the internet, but commonly with missing or noisy sensor information. To prepare this hidden treasure for “ready-to-use” status, determining missing location information and camera orientation angles are two equally important tasks. Recent methods have achieved high performance on geo-localization of street-view images by cross-view matching with a pool of geo-referenced satellite imagery. However, most of the existing works focus more on geo-localization than estimating the image orientation. In this work, we re-state the importance of finding fine-grained orientation for street-view images, formally define the problem and provide a set of evaluation metrics to assess the quality of the orientation estimation. We propose two methods to improve the granularity of the orientation estimation, achieving 82.4% and 72.3% accuracy for images with estimated angle errors below 2° for CVUSA and CVACT datasets, corresponding to 34.9% and 28.2% absolute improvement compared to previous works. Integrating fine-grained orientation estimation in training also improves the performance on geo-localization, giving top 1 recall 95.5%/85.5% and 86.8%/80.4% for orientation known/unknown tests on the two datasets.

CCS CONCEPTS

• **Computing methodologies** → *Scene understanding*; • **Information systems** → **Information extraction**; **Image search**.

KEYWORDS

cross-view matching; camera orientation estimation; street-view imagery; satellite imagery; geo-localization

1 INTRODUCTION

Photos not only contain memories, but also provide us a brand new way to learn and perceive the world through others’ eyes, to find

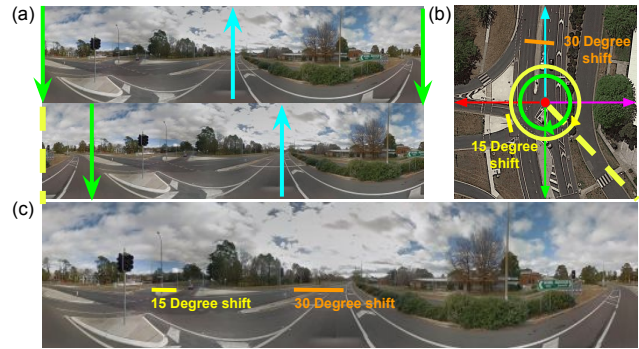


Figure 1: (a) Street-view image queries with 0° and 315° clockwise misalignments, (b) Geo-referenced satellite imagery as the reference for cross-view matching, and (c) Visualization of angle misalignment on a sample street-view image.

details that one may have overlooked earlier, and to share emotions and knowledge with the community. With advances in hardware, personal high-quality cameras have become much more affordable. Many creators are keen on sharing photos on the internet. The captured images may not be as carefully calibrated as if they were taken by a dedicated multi-sensor system (e.g., Google Street View vehicles), but the sheer volume of crowdsourced images surely provides rich information. If we can efficiently estimate the missing meta information (e.g., geo-location, camera orientation) of those images and calibrate them for “ready-to-use” status, this enormous hidden treasure can help on various downstream tasks, e.g., map information extraction [5, 28, 55], car navigation and tracking [2, 17, 22, 31, 33], UAV positioning [24, 27], hazard detection [1, 22, 29, 46], social studies [47]. To accomplish this goal, we must carry out three tasks: (a) adjusting the image upright [20], (b) finding the location, and (c) estimating the viewing angle of the camera.

Image-based geo-localization is a line of study aiming at inferring the camera location of street-view images. Among various geo-localization approaches, cross-view geo-localization uses geo-referenced aerial images (mostly satellite imagery). Given a street-view query image (Figure 1(a)), the system finds the most similar match in a pool of satellite images (Figure 1(b)), and then takes the satellite image center as the localization result. Thanks to its image

retrieval nature, cross-view matching with satellite imagery can be applied in large-scale searches and gives promising results.

However, as a full decade has passed, finding only the location no longer satisfies the requirement to explore the full potential of street-view images. We encourage the community to embrace a more challenging task of *estimating the fine-grained camera orientation of street-view images* to extend the overall objectives for three reasons: 1) With the accurate camera orientation, information extracted from street-view images, especially from using single-image algorithms (e.g., depth estimation, object detection), enables a wider range of real-world applications, e.g., map creation, augmented reality, navigation. In practice, even a very small misalignment in orientation can propagate a large shift to the physical position of objects detected in images. For example, Figure 1 (c) shows that an orientation error of 15° is large enough to mislocate an exit to another lane; an error of 30° is sufficient to mistakenly assign attributes to the reverse direction of the road.

2) Nowadays, crowdsourced high-quality 360° or wide-angle images can be taken by semi-professional 360° cameras or even by phones. These images are usually not carefully calibrated. It is more likely that the orientation information is missing but a rough location is labeled, rather than vice versa. Hence, the problem of finding the location of street-view images assuming the orientation is known is no longer realistic.

3) After surveying recent studies, we found that the performance of cross-view geo-localization is slowly reaching saturation. Based on our experiments, we observe that by introducing a finer granularity to orientation estimation, the performance of geo-localization can be further improved. We hypothesize that the saturation of performance is reached not because of the representation power of the networks, but a lack of precision in orientation to align two images. Finding fine-grained orientation could also potentially improve the performance of geo-localization of crowdsourced images.

Only a few studies have made progress or introduced new ideas on using the orientation characteristic [9, 25, 36, 45, 56, 61]. Even fewer evaluates the orientation estimation result along with the geo-localization task [36, 45, 56, 61]. To the best of our knowledge, Shi *et al.* [36] is the only work taking orientation prediction as the main problem to solve for large scale searching. However, we found the granularity of the estimation could be improved to better fit real-world use cases and the evaluation metrics do not give enough clarity. Hence, in this work, we formally define the problem and propose a set of metrics for evaluating the fine-grained estimation of camera orientation of street-view images. In summary, our contributions lie in the following aspects:

- Define a south-aligned orientation alignment coordinate and a continuous absolute angle error coordinate for orientation estimation in cross-view matching with satellite imagery.
- Propose two methods to enhance the granularity of orientation estimation of street-view images without introducing any additional learnable parameters.
- Propose a set of metrics for orientation estimation, which is easier to understand and gives better clarity for real-world use-cases.
- Demonstrate that by incorporating fine-grained orientation estimation, the performance of geo-localization can be improved.

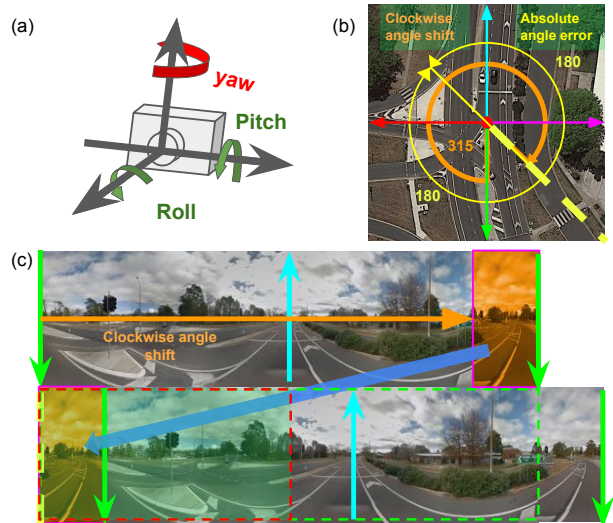


Figure 2: (a) Camera angles, (b) South-aligned reference coordinate for orientation shift, and (c) Visualization of rotation applied on images to create orientation misalignment.

2 FINE-GRAINED ORIENTATION ESTIMATION

2.1 Preliminaries

Prior works on geo-localization [3, 6, 23, 33, 41, 49] leverage on different geo-referenced data sources, e.g., GIS map images. In more recent years, [45] forms this task as an image retrieval problem that matches street-view image queries with geo-referenced satellite images and becomes one of the mainstream approaches for street-view imagery geo-localization. Given an upright street-view image I_g (Figure 2 (c) top) and a set of geo-referenced satellite imagery (Figure 2 (b)), a system shall identify the satellite image I_s at the same location as I_g from a pool of satellite image candidates. The center location of I_s is assigned to be the location of I_g .

Besides geo-localization, finding accurate camera orientation is the other critical task to prepare street-view images for “ready-to-use” status. Figure 2 (a) shows the three camera angles required for calibration. The pitch and roll angle along with other camera distortion can be corrected by methods like [20]. After such corrections, the street-view images are upright and only left the yaw angle, the orientation, for estimation. In the commonly used datasets, the orientation of the street-view image is usually north-aligned, which means the center column of the image points to the Geographic North Pole (marked by the cyan arrow in Figure 2 (c) top) to ensure it is aligned with the north direction of the geo-referenced satellite imagery (north marked by the cyan arrow in Figure 2 (b)). It is commonly known that geo-localization obtains better performance if the orientations of the street-view images are known. However, only a few works on geo-localization [36, 45, 61] propose new initiatives on orientation estimation. Among them, only [36, 61] assign dedicated components to extract the orientation and use the estimated orientation explicitly in the geo-localization steps. We found each previous work [25, 36, 45, 61] has a slightly different definition of the orientation misalignment and error. Therefore, we provide a unified definition that could be beneficial for future works.

Table 1: Different methods to rotate and create misalignment.

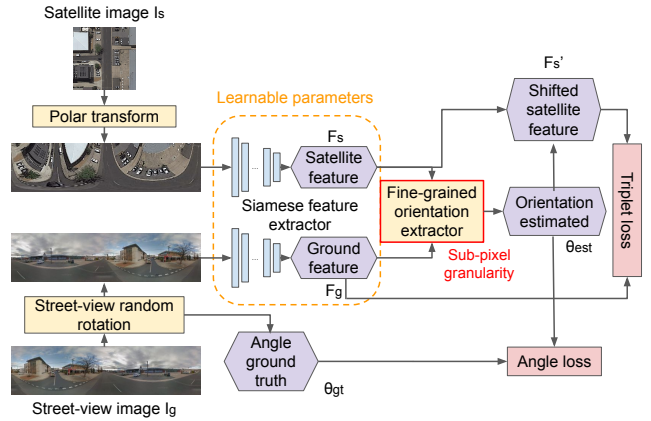
Methods	Rotation on	Alignment	FOV invariant
DSM [36]	Street-view	North	
Zhu <i>et al.</i> [61]	Satellite	South	✓
Ours	Street-view	South	✓

2.2 Problem Formulation

2.2.1 Problem statement. Given a set of upright street-view images $\mathcal{I}_g = \{I_g\}$ and a set of geo-referenced satellite images $\mathcal{I}_s = \{I_s\}$, which are paired and cropped at the same location of their paired street-view image, an orientation misalignment θ_{gt} is created for each street-view and satellite pair following the reference coordinate in section 2.2.2. For each street-view query image I_g , the similarity and orientation θ_{est} between the query I_g and every satellite image candidate in \mathcal{I}_s are estimated. The satellite candidates are ranked by their similarity. The center location of the top-1 satellite image and the estimated orientation with the correct match are extracted as the estimated location and orientation of the query image I_g . We aim to reduce the error between the estimated orientation θ_{est} and θ_{gt} (absolute error coordinate in section 2.2.3), while maintaining or improving the recall of geo-localization.

2.2.2 Reference coordinate for angle shift. To create the misalignment between the street-view image and geo-referenced satellite image, we adapt the augmentation method from [36] to randomly shift the street-view images clockwise and record this angle shift θ_{gt} in a south-aligned reference coordinate. Figure 2(c) shows an example of shifting the street-view image 315° clockwise. Semantically, the augmentation crops the right-most part outside the shifting angle (in the orange shade) and stitches it to the left-most column of the street-view image, and then crops the field of view (FOV) required for the output. In Figure 2 (c), red box shows FOV of 180°, green box shows FOV of 360°. Pseudo-code of rotation and cropping is given in the supplementary materials. Although the original image pairs are north-aligned, we choose the south alignment as the reference, namely the alignment between the first column of the image to the south direction of the satellite image (marked in green arrows in Figure 2). This change is made for images with limited FOV. After cropping, the center column is shifted left-wards and is no longer aligned with the angle shift ground truth θ_{gt} . For example, in a north-aligned coordinate, if a 360° image is shifted by 90 degrees clockwise and cropped to FOV of 180°, the angle shift between the center column and the north direction becomes 45 degrees; if crop to 120°, the angle shift becomes 30 degrees. Table 1 shows different methods for creating misalignment. Compared to DSM [36], our method is FOV invariant, θ_{gt} is consistent regardless of the FOV. Compared to [61], rotating street-view image is easier to implement and our method avoids losing the corners of satellite images because of rotation and distortions caused by interpolation.

2.2.3 Reference coordinate for angle error. We propose to calculate the absolute angle error between the estimated angle shift θ_{est} and ground truth angle shift θ_{gt} . Centered to the θ_{gt} , the errors count up to 180 degrees to the opposite direction (Figure 2 (b)). Compared to using the $[0, 360]$ clockwise or $[-180, 180]$ angle error in [45, 56, 61], the absolute angle error coordinate has the following advantages:

**Figure 3: Overall architecture for geo-localization and orientation estimation. Example shows with 360° FOV.**

- Avoid a sudden change of 360 degrees around the border case in 360° clockwise system ($0 \leftrightarrow 360$) and $[-180, 180]$ system ($-180 \leftrightarrow 180$). Our absolute error coordinate is continuous everywhere, being more natural for defining the angle loss function.
- More fair to compute angle errors. For example, when the ground truth $\theta_{gt} = 0^\circ$ and two estimations are $\theta_{est1} = 170^\circ$ and $\theta_{est2} = 240^\circ$. In a 360° system, the angle error for θ_{est1} is 170° and for θ_{est2} is 240°, although θ_{est2} is closer to θ_{gt} with an absolute error of 120°. The system shall favour θ_{est2} instead of θ_{est1} .
- Easier to calculate angle error from two angles shifts given in the south-aligned coordinate. Given θ_1 and θ_2 in south-aligned coordinate, their angle difference can be calculated as:

$$\theta_{diff} = 180^\circ - \left| |\theta_1 - \theta_2| - 180^\circ \right|. \quad (1)$$

2.3 Method

We adapt the architecture from DSM [36] and proposed two different approaches to obtain fine-grained orientation estimation without introducing any additional learnable parameters. On top of the commonly used triplet loss [45], we defined a new angle loss based on the absolute angle error system (see Section 2.2.3) to learn the angle shift explicitly.

2.3.1 Overview. Figure 3 shows the overall architecture of our geo-localization and orientation estimation system.

Pre-processing: Before passing the input images to the feature extractors, the following pre-processes are applied to street-view images and satellite images respectively:

- In training, street-view images are randomly rotated to introduce orientation misalignments, following section 2.2.2. The ground truth shift in feature space w_{gt} is recorded to calculate the angle loss and orientation estimation accuracy, where $\theta_{gt} = w_{gt}/width(F_s) * 360^\circ$ and F_s is the extracted feature from satellite images.
- Satellite images are *polar-transformed* [36] to a similar viewing point and size as the street-view images to physically reduce the gap between street-view and satellite view images. Figure 3 left top shows the effect of polar transformation.

Feature extraction: The pre-processed satellite and street-view images are sent to *Siamese feature extractors* (in the middle of Figure 3), which are modified based on VGG16 [39]. Following [36], the extractors consist of the first 10 layers of VGG16 and 3 additional convolutional layers to further compress the feature maps on the vertical axis. The last three layers have an output feature depth of [256, 64, 16] and stride [(2, 1), (2, 1), (1, 1)] in the vertical and horizontal axes. For full 360° inputs with size [128, 512, 3], two feature maps F_s and F_g with a size of [4, 64, 16] in [H, W, C] are extracted respectively. The two branches have the same architecture without weight sharing.

Fine-grained orientation estimation: The extracted features F_s and F_g are processed by the fine-grained orientation extractor to infer the sub-pixel level angle shift θ_{est} . Then the satellite features F_s are shifted and cropped (F'_s) to be aligned with the street-view features F_g in orientation and FOV. The output features F'_s and F_g are used to calculate the triplet loss. Moreover, an angle loss is used to provide direct supervision on the orientation estimation. During inference, if the orientation between satellite and street-view is known ($\theta_{\text{gt}} = 0$), the orientation extractor is not used, only cropping of F_s to have the same FOV is applied; if the orientation is unknown, the fine-grained orientation extractor finds the alignment. Shifting and cropping of F_s are applied. Given a query street-view image, the feature similarities between the query and all possible satellite candidates are calculated along with the orientation estimation.

2.3.2 Fine-grained orientation extractor. To find fine-grained orientation (at a sub-degree level), we propose two methods to increase the granularity of the estimation without increasing the number of learnable parameters, compared to DSM [36]. After obtaining the features F_s and F_g , the cross-correlation is calculated as:

$$(F_g \star F_s)[w] = \sum_{m=1}^{W_g} F_g[m] F_s[(m+w)_{\text{mod}} W_s], \quad (2)$$

where $F_{g/s}[m]$ is a slice of features at horizontal position m across all height and channels. W_s and W_g are the width of F_s and F_g . The position with the highest cross-correlation value is taken as the estimated angle shift w_{est} in the feature space. As our input images have a width of 512 pixels, the shifting unit is about 0.7 degree (360°/512 pixels). However, F_s and the cross-correlation result (Equation 2) only have a width of 64 pixels, which makes the orientation extractor have a maximum resolving power of 5.625 degree (360°/64 pixels). The granularity of the result surely cannot recover the actual angle shift for our study and is also not enough for real-world applications. To refine the granularity of the estimation, we proposed two approaches.

Feature interpolation (FI): Following algorithm 1, both F_s and F_g are interpolated with a scaling factor S before calculating the fine-grained cross-correlation curve. In our implementation, we increase the granularity by 10 times. The bin number with the maximum cross-correlation curve is extracted and is divided by S to obtain sub-pixel level estimation w_{est} . The resolving power of the model is refined to 0.5625 degree (360°/640 pixels).

Curve smoothing (CS): Following algorithm 2, the cross-correlation curve $(F_g \star F_s)[w]$ is calculated with the original resolution (64 bins). To smooth the curve with scaling factor $S = 10$, the coarse cross-correlation curve is transformed to frequency domain with Fast Fourier Transform (FFT) and zero-padded of $(S - 1)$ times to

Algorithm 1: Feature Interpolation (FI)

Input: street-view features F_g , satellite features F_s , scaling factor S .
Output: Estimated orientation in feature space w_{est}
 $F_g^s = \text{interpolate}(F_g, S)$, $F_s^s = \text{interpolate}(F_s, S)$
 $(F_g^s \star F_s^s)[w] = \text{cross-corr}(F_g^s, F_s^s)$ // eqn (2)
 $w^s = \max_{\text{position}}((F_g^s \star F_s^s)[w])$ // find shift with max value
 $w_{\text{est}} = w^s / S$ // get sub-pixel position
return w_{est}

Algorithm 2: Curve Smoothing (CS)

Input: street-view features F_g , satellite features F_s , scaling factor S .
Output: Estimated orientation in feature space w_{est}
 $(F_g \star F_s)[w] = \text{cross-corr}(F_g, F_s)$ // coarse curve
 $((F_g \star F_s)[w])_{\text{fft-padded}} = \text{zero-padding}(\text{FFT}((F_g \star F_s)[w]), S)$
 $((F_g \star F_s)[w])_{\text{smooth}} = \text{IFFT}(((F_g \star F_s)[w])_{\text{fft-padded}})$
 $w^s = \max_{\text{position}}(((F_g \star F_s)[w])_{\text{smooth}})$
 $w_{\text{est}} = w^s / S$ // sub-pixel position
return w_{est}

the middle of the curve:

$$\text{ZP}(F[w], S) = \text{Concat}(F[0:\text{int}(W/2)], \\ \text{zeros}[0:(S-1)W], F[\text{int}(W/2)+1:]),$$

where W is the width of the $F[w]$. The output of zero-padding is again converted back by Inverse FFT (IFFT). The fine-grained orientation extractor with CS has a resolving power of 0.5625 degree.

Both CS and FI provide the flexibility to adjust the granularity of the orientation extraction via the changeable scaling factor.

2.3.3 Objective functions with angle loss. To have the direct supervision on angle estimation, we propose an angle loss based on the absolute angle error (section 2.2.3). Given the ground truth orientation in feature space w_{gt} , the estimated orientation w_{est} and the width of the feature map space W , the angle loss is given as:

$$L_{\text{angle}} = (0.5W - ||w_{\text{gt}} - w_{\text{est}}| - 0.5W|) / 0.5W, \quad (3)$$

which is equivalent to the rate of the angle error to the maximum error of 180°. Note that this loss is only applied to matched pairs.

For the geo-localization task, we utilize the commonly used weighted soft-margin triplet loss [17, 35, 36, 38]. Given a triplet consists of an anchor query image A in one view, the positive sample P (correct match) and a negative sample N in the other view, the feature (F_A) extracted from A shall have a smaller distance to the shifted and cropped feature (F'_P) from the P than the shifted and cropped feature (F'_N) from N . We take the cosine distance between features in our implementation. The loss function is given as:

$$L_{\text{match}} = \ln(1 + \exp(\alpha(D(F_A, F'_P) - D(F_A, F'_N)))) \\ D(F_1, F_2) = 2(1 - \cos(F_1, F_2)), \quad (4)$$

where the $\alpha = 10$, following [36]. For a batch size of B , each query can form $(B - 1)$ triplets. In each matching direction (street \rightarrow satellite or satellite \rightarrow street), $B(B - 1)$ triplets are constructed. We enforce the matching on both directions and have totally $2B(B - 1)$ triplets in each mini-batch. The overall objective function is:

$$L = L_{\text{match}}(A, P, N) + \beta L_{\text{angle}}(A, P). \quad (5)$$

2.4 Metrics

Few metrics have been proposed to evaluate the accuracy of orientation estimation. [45, 56, 61] visualized a histogram of estimation error in the range $[-180^\circ, 180^\circ]$, with granularity around 7 to 10 degrees. [61] gives the percentage of images with estimation error within $[-3.5^\circ, 3.5^\circ]$. [36] defines two metrics: 1) the accuracy of the estimations within an error of $\pm 10\%$ of FOV. 2) median of the angle errors of images that are correctly geo-localized (recall@top1). Median is used instead of mean because of some images are estimated to the opposite direction with an error of 180° . This large error has a huge impact on the mean error, but may not have a large impact on the localization. To evaluate the angle error independently from the localization and to provide more clarity on fine-grained orientation estimation for downstream tasks, we propose the following orientation-centric metrics.

2.4.1 Fine-grained histogram. A histogram $H(\theta)$ at 1° granularity is calculated for the absolute angle errors. For every image in the test set, given the ground truth θ_{gt} and the estimation θ_{est} :

$$\theta_{err} = 180^\circ - \left| |\theta_{gt} - \theta_{est}| - 180^\circ \right|, \quad (6)$$

$$H(\theta_i) = H(\theta_i) + 1, \quad \text{where } \theta_i - 1 \leq \theta_{err} < \theta_i.$$

With the fine-grained histogram, 1-to-1 visual comparison between models and the accumulated accuracy curve at any specific degree can be retrieved easily. It shows the distribution and reliability of the orientation estimation, which are crucial for downstream tasks.

2.4.2 Mean angle error. The mean of angle errors of all test images is calculated to evaluate the orientation performance independently on geo-localization for two reasons: 1) There exist alternative sources to obtain location-tag, e.g., social media, and the orientation estimation remains to be the bottleneck for downstream tasks. Any missing orientation information gives the testing images a 180° uncertainty. 2) A 180° error may not affect the geo-localization result, but could be the worse case for many downstream tasks, e.g., navigation. Hence, the mean is used to calculate the error linearly for the entire test set.

2.4.3 Accuracy below specific threshold. The accuracy of test images with an estimation error below a specific threshold is calculated. For a given fine-grained histogram $H(\theta)$ (Equation 6), the rate below x° is given as:

$$r@x^\circ = \frac{\sum_{i=1}^x H(\theta_i)}{\sum_{i=1}^{180} H(\theta_i)}. \quad (7)$$

With these metrics, the users can decide whether the estimated orientation fits the downstream tasks, which usually come with a tolerance of orientation errors.

3 EXPERIMENTAL SETTINGS

3.1 Datasets and Metrics

We evaluate the orientation estimation and geo-localization on two commonly used datasets, CVUSA [50] and CVACT [25]. Both datasets contain 35,532 training street-satellite matched pairs and 8,884 test pairs. All images are angle-aligned. At the training time, random shifting and cropping (if with limited FOV) are applied to street-view images. In testing, we followed the orientation shift

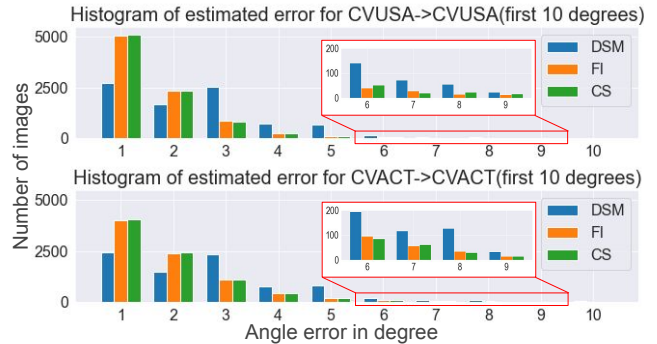


Figure 4: Histogram of angle errors for the best instance of each model on 360° image test. Each set has 8,884 images.

given to each matched pair in [36]. Note that the two datasets are collected in the US and Australia separately and have a non-negligible domain shift. CVUSA contains a mix of commercial, residential, suburban, and rural areas and CVACT leans towards urban/suburban styles. Additionally, the satellite images in CVUSA have a higher ground coverage but a lower resolution than CVACT, which introduces another substantial domain shift. All street-view images and polar-transformed satellite images are resized to $[128, 512]$ pixels in height and width. To evaluate the performance of orientation estimation, mean angle error, $r@2^\circ$, $r@5^\circ$ are used. Visualization of angle error histogram is presented to compare the differences among models. To demonstrate the improvement in geo-localization brought by fine-grained orientation estimation, recall at the top 1 sample ($r@1$) is used for known/unknown orientation test. Additionally, model generalization test results in across and mixed dataset setting are shown in the supplementary materials.

3.2 Implementation Details

All our models and our re-implementation of DSM [36]* are trained with unknown orientation. The first 10 layers of the VGG16 based feature extractors use the pre-trained weights on ImageNet [12] and the last three layers are initialized randomly. Note that in our model all parameters are learnable, while the first 10 layers of DSM are frozen. For fair comparison, batch size B is set to 32 as [35, 36, 48, 52, 57]. We use Adam [21] optimizer with an initial learning rate of $11e^{-5}$, learning rate decrease on plateau is applied with factor 0.5, patience 8. The maximum training time is set to 200 epochs and the early stopping threshold is 30 epochs. For unknown orientation, images can rotate up to 360° . The rotation unit is about 0.70° , corresponding to the shift in one pixel of the input image. The weight for angle loss $\beta=0.3$. The average results of three instances are reported in the following sections, if not otherwise specified.

4 RESULTS

4.1 Fine-grained Orientation Estimation

Table 2 shows the performance of our models on orientation estimation on 360° images along with previous studies [36, 56, 61]. As only a few works report their results on orientation estimation and use different metrics, we re-implement DSM [36] to conduct a full comparison using the newly proposed metrics. The re-implemented

Table 2: Orientation estimation on two datasets. The baseline DSM[36]* is used to compute the gain in the brackets.

Model	Mean error ↓	r@2° (%)	r@5° (%)	Mean error ↓	r@2° (%)	r@5° (%)
CVUSA			CVACT			
Zhai [56]	-	≤15	-	-	-	-
Zhu [61]	-	≤24	-	-	-	-
DSM [36]*	5.29°	47.49	93.25	6.26°	44.13	88.31
Ours (FI)	3.78°	82.13	96.77	4.88°	70.87	92.29
Gain	(1.51°)	(34.64)	(3.52)	(1.38°)	(26.74)	(3.98)
Ours (CS)	3.77°	82.42	96.75	4.75°	72.28	92.43
Gain	(1.52°)	(34.93)	(3.50)	(1.51°)	(28.15)	(4.12)

DSM [36]* is used as the baseline to calculate the improvement shown in the bracket. Both our models, FI and CS, show significant improvement in the mean error, r@2° and r@5° for all test cases.

Both datasets have a similar mean error improvement of about 1.38° to 1.52° from their original mean error of 5.29° and 6.26°. However, CVUSA observed higher absolute improvement on r@2° (about 35%) than CVACT (about 28%). Comparing the histogram visualized in Figure 4, the error distribution of CVUSA is further pushed to the lower angle error region than the distribution of the CVACT results. Around 57% of the test dataset of CVUSA obtained an orientation estimation with an error below 1°, which is around 45% for CVACT. For CVACT, some test cases that are not pushed below the 2° error region are still successfully reduced within 5°. We hypothesize that the CVUSA dataset contains a larger portion of suburban, rural areas than CVACT, which leads the images in CVUSA naturally to have less obvious features, such as buildings, to leverage. This makes the precise orientation estimation has more influence on CVUSA than CVACT.

Between FI and CS, FI interpolates the coarse feature maps with a large scaling number to generate a fine-grained correlation curve with new values, while CS obtains sub-pixel correlation curve values by smoothing the original curve. From our experiment results in Table 2, CS obtains slightly better results than FI on orientation extraction. However, FI gives a more fundamental fine-grained orientation curve generation. It could be useful when prior knowledge of the rough orientation is available, which can be added to the street-view features before the orientation curve is generated.

4.2 Geo-localization

Finding fine-grained orientation does not only provide additional orientation information but also improves the performance of geo-localization. We evaluate the geo-localization result of our models in known/unknown orientation tests. The r@1 of CVUSA and CVACT are shown in Table 3. Note that the performance of the best instance of our FI, CS and DSM [36]* are reported to have a fair comparison. Compared to DSM [36]*, r@1 for known/unknown orientation test on CVUSA improved by 1.93%, 4.70% for FI and 1.80%, 4.64% for CS; on CVACT are improved by 2.91%, 5.17% for FI and 2.34%, 5.55% for CS. Additional results on across dataset and mixed dataset tests and visualization of the top 5 best matched and worst mismatched cases are shown in the supplementary materials.

We achieves better r@1 than all existing methods; especially on CVACT obtaining absolute improvement of 1.66% and 2.66% on

Table 3: Evaluation on geo-localization for the two datasets. The best results of FI, CS and DSM [36]* are reported.

Model	known r@1 (%)	unknown r@1 (%)	known r@1 (%)	unknown r@1 (%)
CVUSA		CVACT		
CVM-NET [17]	22.47	-	20.15	-
Liu & Li [25]	40.79	-	46.96	-
CVFT [38]	61.43	-	61.05	-
SAFA [35]	89.84	-	81.03	-
LPN-SAFA [48]	92.83	-	83.66	-
DSM [36]*	93.57	80.75	83.88	75.24
L2LTR [52]	94.05	-	84.89	-
GAN-SAFA [42]	92.56	-	83.28	-
SSANET [57]	91.52	-	84.23	-
SEH VGG16 bs 30 [16]	94.46	-	-	-
SEH VGG16 bs 120 [16]	95.11	85.36	84.75	78.13
SEH FCANet18 bs 120 [16]	95.04	85.37	85.13	77.41
TransGeo [60]	94.08	-	84.95	-
Ours (FI)	95.50	85.45	86.79	80.41
Ours (CS)	95.37	85.39	86.22	80.79

known and unknown orientation test, without implementing additional sampling strategy or computational expensive architecture. Note that SEH [16] and our models have the same origin from DSM, its work on sampling strategies is in another disentangled research direction. The two methods do not contradict each other and can be applied together with proper adaptation.

4.3 Ablation Study

4.3.1 Location matched vs all test images. DSM [36] analyze the orientation estimation on the test images that are corrected geo-localized, while [45, 56] evaluates the orientation estimation independently from geo-localization. Both methods have valid assumptions, hence we compare the results when only the location-matched images or all test images are evaluated. On top of testing the trained models on their own test set, Table 4 also includes the performance in across dataset tests, namely tests on the images from another domain, to demonstrate the difference in results by using the two approaches. In Table 4, the best instance of FI CVACT and CS CVUSA is shown, ‘all’ means the results of all test images; ‘matched’ means the results of only the matched images; ‘matched to all’ means the results of the matched cases divided by the number of images of the full test set (8,884 images). After removing unmatched cases, the mean error drops drastically, especially for across dataset tests. The r@2° also increases for all tests. Both indicate the images with good geo-localization results have a better orientation estimation in general. However, if consider orientation estimation as an individual problem, any missing estimation given the test images a 180° uncertainty, filtering results based on the location correctness can end up having a very low percentage of correctly estimated images in the full dataset. For across dataset tests, r@2° (matched to all) drops to 9.02% and 12.69%, although the models have the ability to give high-quality orientation to 57.09% and 55.94% of the full test images. Figure 5 shows the majority of

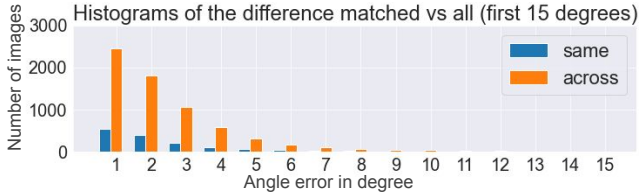


Figure 5: Histogram of the difference between matched cases and all cases for CVACT same/across dataset tests. Most of the removed results are with good orientation estimation.

Table 4: Orientation estimation evaluated on all test data or location matched data. Matched to all means the result evaluated on matched cases to the full dataset, 8,884 images.

	CVACT-> CVACT	CVUSA-> CVUSA	CVACT-> CVUSA	CVUSA-> CVACT
unknown r@1	80.41%	85.39%	12.84%	19.43%
mean error (all)	4.79°	3.65°	18.28°	13.00°
mean error (matched)	1.85°	1.96°	2.98°	2.27°
r@2 (all)	72.60%	83.87%	57.09%	55.94%
r@2 (matched)	77.03%	86.15%	70.20%	65.30%
r@2 (matched to all)	61.94%	73.56%	9.02%	12.69%

the removed cases obtain a high to medium quality orientation estimation. Mislocated images are not necessarily having low-quality orientation estimation. Additionally, evaluating only on location-matched images can lead to an unfair comparison, e.g., a model can trick the evaluation by having only one correctly located image with a perfect estimated orientation. Hence, we believe the evaluation of orientation estimation shall be independent of geo-localization, unless it is for specific use cases.

4.3.2 *Fixed parameters, angle loss, fine-grained.* The parameters in the first 10 layers of the baseline model DSM [36] are fixed. For a fair comparison, Table 5 shows the average performance for 5 different settings on both datasets. DSM [36]* indicate our re-implementation of DSM, DSM (all) refers to the model with all parameters unfixed. ‘AL’ refers to angle loss, FI and CS refer to the two methods we proposed for fine-grained orientation estimation. After releasing all parameters, the performance in all metrics improved compared to baseline. Adding angle loss to DSM (all) alone did not bring many additional benefits as the granularity of the prediction is still at a coarse level. After increasing the granularity, models with ‘AL’ + ‘FI’/‘CS’ show substantial improvements in orientation estimation and perform better on geo-localization for both datasets. The full result of different training settings and angle loss weight is given in the supplementary materials.

4.3.3 *Limited FOV.* We test on images with 180° (fish-eye camera) and 90° (wide-angle camera). The first test uses models trained on 360° images to simulate the situation when a model is trained on well collected 360° images, but the test images are crowdsourced with limited FOV. Table 6 shows the average performances of FI models on CVACT. The absolute improvements to our re-implemented baseline DSM [36]* are given in the brackets. For geo-localization unknown r@1, our result has a 9.60% and 6.83% improvement for 180° and 90° tests. Recent work SEH-VGG16 [16] reports r@1 of 45.99% and 14.06% on the same test. For the orientation estimation,

Table 5: Performance of DSM [36]*, DSM (all), and models with AL (angle loss), FI and CS.

Model	known r@1 (%)	unknown r@1 (%)	Mean error ↓	r@2° (%)
CVUSA				
DSM [36]*	93.29	80.54	5.29°	47.49
DSM (all)	94.99	84.30	4.53°	50.76
DSM (all) + AL	94.90	84.76	4.76°	47.20
DSM (all) + AL + FI	95.29	84.98	3.78°	82.13
DSM (all) + AL + CS	95.27	85.19	3.77°	82.42
CVACT				
DSM [36]*	83.90	75.14	6.26°	44.13
DSM (all)	86.06	80.09	5.67°	46.07
DSM (all) + AL	86.15	80.04	5.56°	45.25
DSM (all) + AL + FI	86.59	80.38	4.88°	70.87
DSM (all) + AL + CS	86.29	80.23	4.75°	72.28

Table 6: Performance of models trained on 360° CVACT images and tested on 180°, 90°. The absolute improvements to DSM [36]* are given in the brackets.

FOV	r@1 (%)	Mean error ↓	r@2° (%)	r@5° (%)
180°	56.47 (9.60)	9.48° (2.79°)	51.12 (19.56)	81.85 (8.91)
90°	21.88 (6.83)	21.57° (3.62°)	30.90 (10.92)	55.35 (6.64)

Table 7: CVACT model trained and tested on limited FOV.

FOV	Model	r@1 (%)	Mean error ↓	r@2° (%)	r@5° (%)
180°	DSM [36]*	58.11%	12.31°	25.41%	64.13%
	Ours FI	67.07%	10.26°	34.82%	69.61%
90°	DSM [36]*	16.77%	39.50°	8.22%	23.61%
	Ours FI	21.08%	40.42°	9.01%	21.23%

we observe improvement on all metrics compared to DSM [36]*. However, the performance and the absolute improvements on most of metrics gradually reduced when the FOV is more restricted. The mean error for 90° FOV is nearly one fourth of its FOV and the r@2° declines to less than 50%. This observation is aligned with our intuition that the difficulty of precise geo-localization and orientation estimation increases drastically when the FOV decreases.

Secondly, we test on FI models trained with limited FOV to understand whether images with limited FOV still contain enough information for learning fine-grained orientation estimation. Table 7 present the results of models trained on 180° and 90°. Comparing to the baseline, our model FI gives improvement in most of the metrics, indicating our methods is applicable for limited FOV. The improvement to baselines and performance itself on 180° is much more significant than 90°. This reduction caused by decreased FOV is more drastic in models trained with limited FOV compared to what we observed in full FOV trained models (Table 6). Additionally, besides the unknown r@1 of 180° obtains a higher performance than the model trained with 360°, all other metrics in limited FOV training result in worse performance, especially on orientation extraction. It indicates that missing partial FOV has great influence on both orientation and location extraction. However, its impacts on finding precise image orientation might be more significant than location extraction.

5 FINDINGS AND DISCUSSION

(1) Orientation estimation: our methods improve the orientation estimation performance for both datasets. It has a higher influence on CVUSA, as images in CVUSA have less complex scenes and obvious features. In general, CS obtains slightly better results in our test cases, however, FI gives more fundamental fine-grained orientation curve generation, this could be useful when prior knowledge of the rough orientation is available. (2) Geo-localization: by integrating fine-grained orientation estimation, the trained models obtain higher performance, compared to baseline models. The $r@1$ for both datasets achieve better scores than existing methods. Note that our initiatives on integrating fine-grained orientation estimation are compatible with some recent works, *e.g.*, [16] on sampling strategies. (3) Evaluation: When the street-view images are correctly geo-localized, the orientation estimation has higher precision. However, most of the location-incorrect images still obtain high to medium quality orientation estimation. It is also fairer to evaluate orientation estimation independently from geo-localization. (4) Limited FOV: When a model is trained on 360° images and is tested on limited FOV, the performance of geo-localization and orientation estimation both decrease. The more limited the FOV restricts, the worse the performance is. When a model is trained and tested on a limited FOV, the missing information has higher impacts on fine-grained orientation estimation than geo-localization.

6 RELATED WORK

Because of its unique prospective and large ground coverage, satellite imagery has been used in different geo-information extraction applications [7, 8, 11, 18, 53, 54, 59]. In recent years, satellite imagery-based cross-view matching has become one of the mainstream approaches for street-view imagery geo-localization [9, 16, 17, 25, 30, 32, 35, 36, 38, 40, 42, 44, 45, 48, 50, 52, 57, 60, 61]. It partially solves the task to prepare crowdsourced street-view images for “ready-to-use” status. The main challenge of image-based cross-view matching is to bridge the gap between the two views. Traditional key-point extraction methods, *e.g.*, SIFT [26], do not work on images taken from drastically different viewing angles [3, 13, 41]. *Vo et al.* [45] propose a deep learning based method to extract features from different views by studying triplets. Follow-up works aim to further reduce the gaps between the two views and their contributions can be categorized into three aspects. 1) Enhancing correspondences between two views by introducing new learnable components in the network or transforming images from one view to another view [10, 17, 25, 30, 35, 35, 37, 38, 42, 48, 52, 57, 60]. Advanced techniques, such as NetVLAD [4], spatial transformer layers [19], generative adversarial models [15], attention or vision transformer mechanics [14, 43] are tested. A major breakthrough realized by polar transformation is introduced in [35]. 2) Using data sampler/additional information/augmentations to guide the training [9, 16, 17, 25, 32]. 3) Utilizing orientation estimation. [45] adds an auxiliary loss for angle orientation. [36, 56, 61] find the orientation by correlating extracted features from two views.

Researchers are also looking for more challenging problems. The University-1652 dataset [58] has been introduced to include UAV data as one of the platforms for geo-localization. The VIGOR dataset [62] is provided to refine the precision of geo-localization beyond

image retrieval for large scale searching. Additionally, cross-view matching is also adapted for small scale search in recent works, such as in autonomous driving domain [34, 51] to refine the location and/or orientation when prior knowledge is given.

7 CONCLUSION AND FUTURE WORK

In this work, we formally define the fine-grained orientation estimation of street-view images by cross-view matching with satellite imagery. The aim is to extend the scope of current work on geo-localization and give it a more realistic setting and meaningful goal to fully explore the potential of crowdsourced street-view images. We achieve 82.4% and 72.3% accuracy for images with orientation estimation error below 2° for CVUSA and CVACT. Our results also show that by integrating fine-grained orientation estimation, the performance of geo-localization are improved.

Concurrent works also pursue new initiatives in different directions. We highlight the following potential aspects for future works: (1) Limited FOV. In this work, we have tested geo-localization and orientation estimation with different settings. Among all, finding geo-localization and fine-grained orientation from images with limited FOV is the most challenging problem but also the one with the highest societal impacts. (2) Combining with other data sources. Map rendered imagery can be an additional input or a replacement for satellite imagery. Compared to satellite imagery, map rendered images contain fewer details, but are easier to obtain and have less influence on seasonal/weather conditions. When prior knowledge of location/orientation is available, additional data sources, *e.g.*, GPS, can be used to reduce the searching space for local scale search. (3) Use of metrics. In this work, we evaluate the performance of all test images. However, future works can further explore other extensions of the existing metrics to cater to different task-specific requirements. (4) Beyond image retrieval. Our work assumes satellite images can be densely cropped in the area of interest, hence the camera locations are not far away from the satellite image centers. However, fine-grained location extraction beyond image retrieval is definitely helpful to reduce the sampling density of the satellite images for large scale applications. The new challenge is to extract fine-grained location and orientation at the same time for off-center orientation unknown images without any prior knowledge.

ACKNOWLEDGMENTS

This work was funded by the Grab-NUS AI Lab, a joint collaboration between GrabTaxi Holdings Pte. Ltd. and National University of Singapore, and the Industrial Postgraduate Program (Grant: S18-1198-IPP-II) funded by the Economic Development Board of Singapore.

REFERENCES

- [1] David B Abou Chacra and John S Zelek. 2017. Fully automated road defect detection using street view images. In *2017 14th Conference on Computer and Robot Vision (CRV)*. IEEE, 353–360.
- [2] Pratik Agarwal, Wolfram Burgard, and Luciano Spinello. 2015. Metric Localization Using Google Street View. In *2015 IEEE/RSJ International Conference on Intelligent Robots and Systems (IROS)*. 3111–3118.
- [3] Hani Altwaijry, Eduard Trulls, James Hays, Pascal Fua, and Serge Belongie. 2016. Learning to match aerial images with deep attentive architectures. In *Proceedings of the IEEE Conference on Computer Vision and Pattern Recognition*. 3539–3547.
- [4] Relja Arandjelovic, Petr Gronat, Akihiko Torii, Tomas Pajdla, and Josef Sivic. 2016. NetVLAD: CNN architecture for weakly supervised place recognition. In *Proceedings of the IEEE conference on computer vision and pattern recognition*. 5297–5307.
- [5] Vahid Balali, Armin Ashouri Rad, and Mani Golparvar-Fard. 2015. Detection, classification, and mapping of US traffic signs using google street view images for roadway inventory management. *Visualization in Engineering* 3, 1 (2015), 1–18.
- [6] Mayank Bansal, Harpreet S Sawhney, Hui Cheng, and Kostas Daniilidis. 2011. Geo-localization of street views with aerial image databases. In *Proceedings of the 19th ACM international conference on Multimedia*. 1125–1128.
- [7] Favien Bastani, Songtao He, Sofiane Abbar, Mohammad Alizadeh, Hari Balakrishnan, Sanjay Chawla, and Sam Madden. 2018. Machine-assisted map editing. In *Proceedings of the 26th ACM SIGSPATIAL International Conference on Advances in Geographic Information Systems*. 23–32.
- [8] Favien Bastani, Songtao He, Sofiane Abbar, Mohammad Alizadeh, Hari Balakrishnan, Sanjay Chawla, Sam Madden, and David DeWitt. 2018. Roadtracer: Automatic extraction of road networks from aerial images. In *Proceedings of the IEEE Conference on Computer Vision and Pattern Recognition*. 4720–4728.
- [9] Sudong Cai, Yulan Guo, Salman Khan, Jiwei Hu, and Gongjian Wen. 2019. Ground-to-aerial image geo-localization with a hard exemplar reweighting triplet loss. In *Proceedings of the IEEE/CVF International Conference on Computer Vision*. 8391–8400.
- [10] Rui Cao, Jiasong Zhu, Qing Li, Qian Zhang, Qingquan Li, Bozhi Liu, and Guoping Qiu. 2019. Learning Spatial-Aware Cross-View Embeddings for Ground-to-Aerial Geolocalization. In *International Conference on Image and Graphics*. Springer, 57–67.
- [11] Ilke Demir, Krzysztof Koperski, David Lindenbaum, Guan Pang, Jing Huang, Saikat Basu, Forest Hughes, Devis Tuia, and Ramesh Raskar. 2018. Deepglobe 2018: A challenge to locate the earth through satellite images. In *Proceedings of the IEEE Conference on Computer Vision and Pattern Recognition Workshops*. 172–181.
- [12] Jia Deng, Wei Dong, Richard Socher, Li-Jia Li, Kai Li, and Li Fei-Fei. 2009. Imagenet: A large-scale hierarchical image database. In *2009 IEEE conference on computer vision and pattern recognition*. Ieee, 248–255.
- [13] Daniel DeTone, Tomasz Malisiewicz, and Andrew Rabinovich. 2018. Superpoint: Self-supervised interest point detection and description. In *Proceedings of the IEEE conference on computer vision and pattern recognition workshops*. 224–236.
- [14] Alexey Dosovitskiy, Lucas Beyer, Alexander Kolesnikov, Dirk Weissenborn, Xiuhua Zhai, Thomas Unterthiner, Mostafa Dehghani, Matthias Minderer, Georg Heigold, Sylvain Gelly, et al. 2020. An image is worth 16x16 words: Transformers for image recognition at scale. *arXiv preprint arXiv:2010.11929* (2020).
- [15] Ian Goodfellow, Jean Pouget-Abadie, Mehdi Mirza, Bing Xu, David Warde-Farley, Sherjil Ozair, Aaron Courville, and Yoshua Bengio. 2014. Generative adversarial nets. *Advances in neural information processing systems* 27 (2014).
- [16] Yulan Guo, Michael Choi, Kunhong Li, Farid Boussaid, and Mohammed Benamoun. 2022. Soft Exemplar Highlighting for Cross-View Image-Based Geo-Localization. *IEEE Transactions on Image Processing* 31 (2022), 2094–2105.
- [17] Sixing Hu, Mengdan Feng, Rang MH Nguyen, and Gim Hee Lee. 2018. Cvm-net: Cross-view matching network for image-based ground-to-aerial geo-localization. In *Proceedings of the IEEE Conference on Computer Vision and Pattern Recognition*. 7258–7267.
- [18] Wenmiao Hu, Yifang Yin, Ying Kiat Tan, An Tran, Hannes Kruppa, and Roger Zimmermann. 2021. GeoPalette: Road Segmentation with Limited Satellite Imagery. In *Proceedings of the 29th International Conference on Advances in Geographic Information Systems*. 95–98.
- [19] Max Jaderberg, Karen Simonyan, Andrew Zisserman, et al. 2015. Spatial transformer networks. *Advances in neural information processing systems* 28 (2015).
- [20] Jinwoong Jung, Beomseok Kim, Joon-Young Lee, Byungmoon Kim, and Seungyong Lee. 2017. Robust upright adjustment of 360 spherical panoramas. *The Visual Computer* 33, 6 (2017), 737–747.
- [21] Diederik P Kingma and Jimmy Ba. 2015. Adam: A Method for Stochastic Optimization. In *ICLR (Poster)*.
- [22] Xu Lei, Chenglong Liu, Li Li, and Guiping Wang. 2020. Automated pavement distress detection and deterioration analysis using street view map. *IEEE Access* 8 (2020), 76163–76172.
- [23] Tsung-Yi Lin, Serge Belongie, and James Hays. 2013. Cross-view image geolocalization. In *Proceedings of the IEEE Conference on Computer Vision and Pattern Recognition*. 891–898.
- [24] Tsung-Yi Lin, Yin Cui, Serge Belongie, and James Hays. 2015. Learning deep representations for ground-to-aerial geolocalization. In *Proceedings of the IEEE conference on computer vision and pattern recognition*. 5007–5015.
- [25] Liu Liu and Hongdong Li. 2019. Lending orientation to neural networks for cross-view geo-localization. In *Proceedings of the IEEE/CVF Conference on Computer Vision and Pattern Recognition*. 5624–5633.
- [26] David G Lowe. 2004. Distinctive image features from scale-invariant keypoints. *International journal of computer vision* 60, 2 (2004), 91–110.
- [27] Andrés L Majdik, Damiano Verda, Yves Albers-Schoenberg, and Davide Scaramuzza. 2015. Air-ground matching: Appearance-based GPS-denied urban localization of micro aerial vehicles. *Journal of Field Robotics* 32, 7 (2015), 1015–1039.
- [28] Rama Sai Mamidala, Uday Uthkota, Mahamkali Bhavani Shankar, A Joseph Antony, and AV Narasimhadhan. 2019. Dynamic approach for lane detection using google street view and CNN. In *TENCON 2019-2019 IEEE Region 10 Conference (TENCON)*. IEEE, 2454–2459.
- [29] Mohsen Maniat, Charles V Camp, and Ali R Kashani. 2021. Deep learning-based visual crack detection using Google Street View images. *Neural Computing and Applications* 33, 21 (2021), 14565–14582.
- [30] Krishna Regmi and Mubarak Shah. 2019. Bridging the domain gap for ground-to-aerial image matching. In *Proceedings of the IEEE/CVF International Conference on Computer Vision*. 470–479.
- [31] Krishna Regmi and Mubarak Shah. 2021. Video Geo-Localization Employing Geo-Temporal Feature Learning and GPS Trajectory Smoothing. In *Proceedings of the IEEE/CVF International Conference on Computer Vision*. 12126–12135.
- [32] Royston Rodrigues and Masahiro Tani. 2021. Are These from the Same Place? Seeing the Unseen in Cross-View Image Geo-Localization. In *Proceedings of the IEEE/CVF Winter Conference on Applications of Computer Vision*. 3753–3761.
- [33] Turgay Senlet and Ahmed Elgammal. 2011. A framework for global vehicle localization using stereo images and satellite and road maps. In *2011 IEEE International Conference on Computer Vision Workshops (ICCV Workshops)*. IEEE, 2034–2041.
- [34] Yujiao Shi and Hongdong Li. 2022. Beyond Cross-view Image Retrieval: Highly Accurate Vehicle Localization Using Satellite Image. In *Proceedings of the IEEE/CVF Conference on Computer Vision and Pattern Recognition*. 17010–17020.
- [35] Yujiao Shi, Liu Liu, Xin Yu, and Hongdong Li. 2019. Spatial-aware feature aggregation for image based cross-view geo-localization. *Advances in Neural Information Processing Systems* 32 (2019).
- [36] Yujiao Shi, Xin Yu, Dylan Campbell, and Hongdong Li. 2020. Where am i looking at? joint location and orientation estimation by cross-view matching. In *Proceedings of the IEEE/CVF Conference on Computer Vision and Pattern Recognition*. 4064–4072.
- [37] Yujiao Shi, Xin Yu, Liu Liu, Dylan Campbell, Piotr Koniusz, and Hongdong Li. 2022. Accurate 3-DoF Camera Geo-Localization via Ground-to-Satellite Image Matching. *arXiv preprint arXiv:2203.14148* (2022).
- [38] Yujiao Shi, Xin Yu, Liu Liu, Tong Zhang, and Hongdong Li. 2020. Optimal feature transport for cross-view image geo-localization. In *Proceedings of the AAAI Conference on Artificial Intelligence*, Vol. 34. 11990–11997.
- [39] Karen Simonyan and Andrew Zisserman. 2014. Very deep convolutional networks for large-scale image recognition. *arXiv preprint arXiv:1409.1556* (2014).
- [40] Bin Sun, Chen Chen, Yingying Zhu, and Jianmin Jiang. 2019. Geocapsnet: Ground to aerial view image geo-localization using capsule network. In *2019 IEEE International Conference on Multimedia and Expo (ICME)*. IEEE, 742–747.
- [41] Yicong Tian, Chen Chen, and Mubarak Shah. 2017. Cross-view image matching for geo-localization in urban environments. In *Proceedings of the IEEE Conference on Computer Vision and Pattern Recognition*. 3608–3616.
- [42] Aysim Toker, Qunjie Zhou, Maxim Maximov, and Laura Leal-Taixé. 2021. Coming down to earth: Satellite-to-street view synthesis for geo-localization. In *Proceedings of the IEEE/CVF Conference on Computer Vision and Pattern Recognition*. 6488–6497.
- [43] Ashish Vaswani, Noam Shazeer, Niki Parmar, Jakob Uszkoreit, Llion Jones, Aidan N Gomez, Lukasz Kaiser, and Illia Polosukhin. 2017. Attention is all you need. *Advances in neural information processing systems* 30 (2017).
- [44] Sebastiano Verde, Thiago Resek, Simone Milani, and Anderson Rocha. 2020. Ground-to-aerial viewpoint localization via landmark graphs matching. *IEEE Signal Processing Letters* 27 (2020), 1490–1494.
- [45] Nam N Vo and James Hays. 2016. Localizing and orienting street views using overhead imagery. In *European conference on computer vision*. Springer, 494–509.
- [46] Chaofeng Wang, Sarah Elizabeth Antos, and Luis Miguel Triveno. 2021. Automatic detection of unreinforced masonry buildings from street view images using deep learning-based image segmentation. *Automation in Construction* 132 (2021), 103968.
- [47] Mingshu Wang and Floris Vermeulen. 2021. Life between buildings from a street view image: What do big data analytics reveal about neighbourhood organisational vitality? *Urban Studies* 58, 15 (2021), 3118–3139.

- [48] Tingyu Wang, Zhedong Zheng, Chenggang Yan, Jiyong Zhang, Yaoqi Sun, Bolun Zheng, and Yi Yang. 2021. Each part matters: Local patterns facilitate cross-view geo-localization. *IEEE Transactions on Circuits and Systems for Video Technology* (2021).
- [49] Scott Workman and Nathan Jacobs. 2015. On the location dependence of convolutional neural network features. In *Proceedings of the IEEE Conference on Computer Vision and Pattern Recognition Workshops*. 70–78.
- [50] Scott Workman, Richard Souvenir, and Nathan Jacobs. 2015. Wide-area image geolocalization with aerial reference imagery. In *Proceedings of the IEEE International Conference on Computer Vision*. 3961–3969.
- [51] Zimin Xia, Olaf Booij, Marco Manfredi, and Julian FP Kooij. 2021. Cross-View Matching for Vehicle Localization by Learning Geographically Local Representations. *IEEE Robotics and Automation Letters* 6, 3 (2021), 5921–5928.
- [52] Hongji Yang, Xiufan Lu, and Yingying Zhu. 2021. Cross-view Geo-localization with Layer-to-Layer Transformer. *Advances in Neural Information Processing Systems* 34 (2021).
- [53] Yifang Yin, Wenmiao Hu, An Tran, Hannes Kruppa, Roger Zimmermann, and See-Kiong Ng. 2022. A Context-enriched Satellite Imagery Dataset and an Approach for Parking Lot Detection. In *Proceedings of the IEEE/CVF Winter Conference on Applications of Computer Vision*. 1371–1380.
- [54] Yifang Yin, An Tran, Ying Zhang, Wenmiao Hu, Guanfeng Wang, Jagannadan Varadarajan, Roger Zimmermann, and See-Kiong Ng. 2021. Multimodal Fusion of Satellite Images and Crowdsourced GPS Traces for Robust Road Attribute Detection. In *Proceedings of the 29th International Conference on Advances in Geographic Information Systems*. 107–116.
- [55] Amir Roshan Zamir, Alexander Darino, and Mubarak Shah. 2011. Street view challenge: Identification of commercial entities in street view imagery. In *2011 10th International Conference on Machine Learning and Applications and Workshops*, Vol. 2. IEEE, 380–383.
- [56] Menghua Zhai, Zachary Bessinger, Scott Workman, and Nathan Jacobs. 2017. Predicting ground-level scene layout from aerial imagery. In *Proceedings of the IEEE Conference on Computer Vision and Pattern Recognition*. 867–875.
- [57] Xiuwei Zhang, Xiangchuang Meng, Hanlin Yin, Yixin Wang, Yuanzeng Yue, Yinghui Xing, and Yanning Zhang. 2021. SSA-Net: Spatial Scale Attention Network for Image-Based Geo-Localization. *IEEE Geoscience and Remote Sensing Letters* 19 (2021), 1–5.
- [58] Zhedong Zheng, Yunchao Wei, and Yi Yang. 2020. University-1652: A multi-view multi-source benchmark for drone-based geo-localization. In *Proceedings of the 28th ACM international conference on Multimedia*. 1395–1403.
- [59] Lichen Zhou, Chuang Zhang, and Ming Wu. 2018. D-LinkNet: LinkNet with pretrained encoder and dilated convolution for high resolution satellite imagery road extraction. In *Proceedings of the IEEE Conference on Computer Vision and Pattern Recognition Workshops*. 182–186.
- [60] Sijie Zhu, Mubarak Shah, and Chen Chen. 2022. TransGeo: Transformer Is All You Need for Cross-view Image Geo-localization. In *Proceedings of the IEEE/CVF Conference on Computer Vision and Pattern Recognition*. 1162–1171.
- [61] Sijie Zhu, Taojiannan Yang, and Chen Chen. 2021. Revisiting street-to-aerial view image geo-localization and orientation estimation. In *Proceedings of the IEEE/CVF Winter Conference on Applications of Computer Vision*. 756–765.
- [62] Sijie Zhu, Taojiannan Yang, and Chen Chen. 2021. Vigor: Cross-view image geo-localization beyond one-to-one retrieval. In *Proceedings of the IEEE/CVF Conference on Computer Vision and Pattern Recognition*. 3640–3649.

A SUPPLEMENTARY MATERIALS

A.1 Method to rotate and crop street-view image

The algorithm 3 shows the augmentation to rotate the street-view images and create orientation shift ground truth in feature space. It is adapted from DSM [36], while allowing sub-pixel locations of the ground truth for fine-grained orientation estimation.

Algorithm 3: Shift and crop Street-view Image

Input: Street-view image I , feature map width w , field of view γ .

Output: Shifted image I_{sc} , ground truth alignment w_{gt} .

```

 $w_f = \gamma/360 * w$  //calculate the cropped image width
 $x_{shift} = \text{randint}(0, I.\text{width} - 1)$  //define a random shift
/* shift image */
 $I_s = \text{concat}(I[I.\text{width} - x_{shift} :], I[: I.\text{width} - x_{shift}])$ 
 $I_{sc} = I_s[: w_f]$  // cropped the first  $w_f$  pixels
 $w_{gt} = \text{mod}(((I.\text{width} - x_{shift})/I.\text{width} * w), w)$  //shift in feature map width
return  $I_{sc}, w_{gt}$ 
    
```

A.2 Polar transformation

We used the polar transformation from DSM [36] to pre-process the satellite images. Given a satellite image with the size of (S_s, S_s) , to transform it into a flattened image with the size as street-view image (H_g, W_g) , the pixel relation between satellite coordinate x_i^s, y_i^s and street-view coordinate x_i^g, y_i^g (both coordinate take the left-upper corner as the origin):

$$x_i^s = \frac{S_s}{2} - \frac{S_s}{2} \frac{H_g - y_i^g}{H_g} \sin\left(\frac{2\pi}{W_g} x_i^g\right)$$

$$y_i^s = \frac{S_s}{2} + \frac{S_s}{2} \frac{H_g - y_i^g}{H_g} \cos\left(\frac{2\pi}{W_g} x_i^g\right)$$



Figure 6: Sample images from CVUSA [50] and CVACT [25] dataset. Top 2: CVACT; Bottom 2: CVUSA.

A.3 Sample images for CVACT and CVUSA

Sample images from CVACT/CVUSA are shown in Figure 6. Note that the two datasets are collected in the US and Australia separately and have a non-negligible domain shift. CVUSA contains a mix of commercial, residential, suburban, and rural areas and CVACT leans towards urban/suburban styles. Moreover, the satellite images in CVUSA have a higher ground coverage but a lower resolution than CVACT, introducing another substantial domain shift.

A.4 Histograms for same/against dataset tests

Figure 7, Figure 8 and Figure 9 shows the histograms of the best models of our re-implemented DSM [36]*, FI and CS for same dataset test (last 10°) and across dataset test (first and last 10°).

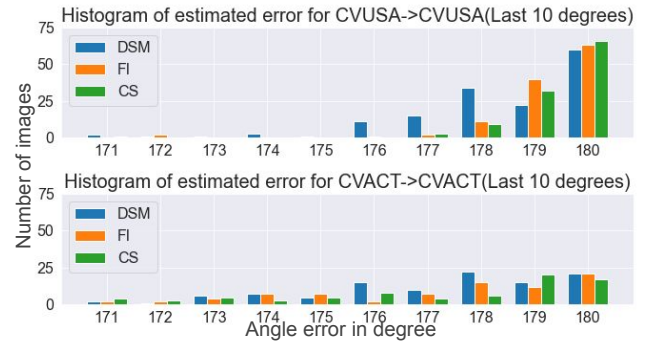


Figure 7: Histogram of angle errors for CVUSA and CVACT on same dataset tests (last 10 degrees).

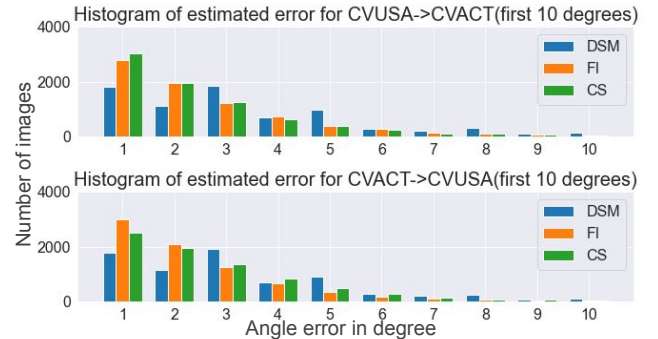


Figure 8: Histogram of angle errors for CVUSA and CVACT on across dataset tests (first 10 degrees).

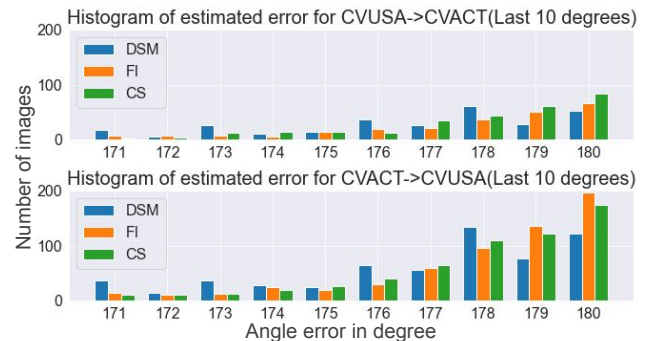


Figure 9: Histogram of angle errors for CVUSA and CVACT on across dataset tests (last 10 degrees).

Table 8: Orientation extraction results in across dataset tests.

Model	Mean error ↓	r@2° (%)	r@5° (%)	Mean error	r@2° (%)	r@5° (%)
CVUSA->CVACT			CVACT->CVUSA			
DSM [36]*	15.48°	32.45	72.18	22.21°	32.40	72.04
Ours (FI)	13.15°	52.94	79.77	19.13°	54.95	81.21
Gain	(2.33°)	(20.49)	(7.59)	(3.08°)	(22.55)	(9.17)
Ours (CS)	13.02°	54.30	80.21	18.61°	54.13	81.73
Gain	(2.46°)	(21.85)	(8.03)	(3.60°)	(21.73)	(9.69)

Table 9: Geo-localization results in across dataset tests. *SAFA[35] across dataset result from [52].

Model	known r@1 (%)	unknown r@1 (%)	known r@1 (%)	unknown r@1 (%)
CVUSA->CVACT		CVACT->CVUSA		
SAFA [35]	30.40	-	21.45	-
DSM [36]*	38.47	18.42	21.68	8.01
L2LTR [52]	47.55	-	33.00	-
Ours (FI)	43.58	20.85	30.29	12.84
Ours (CS)	42.04	19.43	29.06	12.47

A.5 Performance on across dataset tests

For across dataset tests, we train on one dataset and test on the other dataset. For example, in Table 8 and Table 9 CVACT → CVUSA means model trained on CVACT train set and tested on CVUSA test set.

The performance on orientation extraction is shown in Table 8. Because of the domain shift between the two datasets, both test cases have larger mean errors to begin with, compared to same dataset tests. The r@2° have an absolute improvement around 20% to 23% from the original accuracy about 32% for both cases. CVACT → CVUSA obtained better improvements on the mean error (about 3.6°) and r@5° (about 9.7%). Combining the fact that CVACT has a worse initial mean error for across dataset tests, we believe the higher ratio of urban images in CVACT leads the models to leverage the obvious features, e.g., buildings. When such features are missing in the CVUSA, it results in a worse performance than the reversed case (CVUSA→CVACT). By integrating fine-grained orientation estimation in training, the models improve on generalization and transferability and have less dependency on easy features.

For geo-localization, by learning fine-grained orientation estimation, the trained models gain higher generalization and transferability in across dataset tests without implementing additional sampling strategy or computational expensive architecture. Compared to our implementation of the baseline model DSM [36]*, the r@1 for known/unknown orientation for CVUSA→CVACT are improved by 5.11%, 2.43% for FI and 3.57%, 1.01% for CS; for CVACT→CVUSA are improved by 8.61%, 4.83% for FI and 7.38%, 4.46% for CS. Compared to recent works, L2LTR[52] achieves higher performance on known orientation tests, with the usage of ResNet backbone with 12 layers of vision transformers on each view to bridge the gap between two views.

A.6 Performance on mixed dataset tests

Table 10 and Table 11 show the performance of best instance of each model trained on CVACT in a test that the test set of the two datasets are mixed. Besides the metrics used in the main sessions, few new metrics are added to understand the improvements in the sets and their contribution to the overall performance. For r@1, r@2°, r@5° and mean error, we show the breakdown for same dataset (data in CVACT test set) and across dataset (data in CVUSA test set). Additionally, the a hit rate within its own dataset is calculated, which shows the percentage of queries of each dataset choose a satellite candidate from its own satellite pool.

Compared to DSM [36]*: (1) our FI model not only improves the performance of the same test dataset, but also propagates the improvement to across test dataset. For r@5°, mean error, known r@1 and all hit rates, the gains in the across test set are even higher than the same test set. (2) The hit rate for unknown and known orientation tests both obtain more balanced performances and reduce the gap between the same and across test datasets. Our model gives less unfair favors to the training dataset. Both of the results show that learning orientation extraction improves not only the performance of the trained models, but also improves the generalization of the models to be applied in other geo-location/slightly different acquisition settings.

Table 10: Orientation extraction performance of mixed dataset tests on model trained on CVACT.

	Ours FI	DSM [36]*	Gain
r@2°	64.85%	38.70%	26.15%
r@2° (same)	72.60%	44.26%	28.34%
r@2° (across)	57.10%	33.15%	23.95%
r@5°	87.45%	80.60%	6.85%
r@5° (same)	92.54%	88.44%	4.10%
r@5° (across)	82.36%	72.76%	9.60%
Mean error ↓	11.53°	14.22°	2.69°
Mean error (same) ↓	4.79°	6.30°	1.51°
Mean error (across) ↓	18.28°	22.14°	3.86°

Table 11: Geo-localization performance of mixed dataset tests on model trained on CVACT.

	Ours FI	DSM [36]*	Gain
unknown r@1	46.21%	40.99%	5.22%
unknown r@1 (same)	79.90%	74.56%	5.34%
unknown r@1 (across)	12.53%	7.42%	5.11%
unknown hit (same)	97.57%	97.13%	0.44%
unknown hit (across)	95.42%	88.65%	6.76%
known r@1	58.05%	51.96%	6.09%
known r@1 (same)	86.37%	83.35%	3.02%
known r@1 (across)	29.73%	20.57%	9.16%
known hit (same)	98.20%	97.87%	0.33%
known hit (across)	96.69%	91.69%	5.00%

Table 12: Model performance on VIGOR dataset with our CS methods.

	S10 known	S1 unknown	S10 unknown
known r@1	16.99%	20.81%	20.81%
known hit rate	22.86%	28.60%	28.56%
unknown r@1	11.47%	16.67%	16.70%
unknown hit rate	16.34%	24.54%	24.46%
Mean error ↓	36.46°	34.53°	34.51°
r@2°	10.54%	9.80%	11.52%
r@5°	24.21%	27.23%	26.43%

A.7 Large location offset test

In this work, we consider the matched pairs in CVUSA and CVACT are perfectly location aligned. However, the datasets do contain small location translation offsets due to GPS errors *e.g.*, last row of Figure 11, the camera location shall be on the main road instead of the side road, the top 1 prediction is actually closer to the real position. For some extreme cases, the camera locations of the street-view images are off their matched satellite images. *e.g.* first, second and fourth row of Figure 11, the actual camera location drifts off from the matched image (ground truth) and actually is around the top 1 prediction given by our model. Hence, our models tolerate small location offsets.

Although it is out of the scope of this work, we test on the VIGOR (camera locations have large offsets to the satellite image centers) out of curiosity. The result is shown in Table 12. Large offsets indeed demolish the overall performance. But, we found adding fine-grained orientation extraction still improves the performance:

- Training with unknown orientation increases performance on r@1, r@2°, r@5° and mean orientation error, compared to models trained with known orientation.
- Training with a high scaling factor of fine-grained orientation improves the fine-grained orientation extraction, compared to models trained with a lower scaling factor.

A.8 Performance of geo-localization and orientation on two datasets with different configurations.

Table 13 shows the performance with different configurations. The average performance of three instances is reported. In the main paper, angle weight of 0.3 is used.

Table 13: Performance of geo-localization and orientation on two datasets with different configurations.

	angle weight	CVACT -> CVACT					CVACT -> CVUSA				
		known r@1	unknown r@1	Mean error (°)↓	r@2°	r@5°	known r@1	unknown r@1	Mean error(°)↓	r@2°	r@5°
DSM [36]*	-	83.90%	75.14%	6.26	44.13%	88.31%	21.69%	7.90%	22.21	32.40%	72.04%
DSM (all)	-	86.06%	80.09%	5.67	46.07%	89.91%	25.79%	11.00%	20.96	35.05%	75.85%
DSM (all) + AL	0.1	86.12%	80.19%	5.73	43.89%	88.66%	26.46%	11.28%	20.19	35.22%	76.28%
DSM (all) + AL	0.3	86.15%	80.04%	5.56	45.25%	89.42%	26.19%	11.08%	20.57	35.12%	76.08%
DSM (all) + AL	0.5	86.17%	80.14%	5.67	44.08%	88.86%	25.52%	11.00%	20.86	32.76%	73.51%
DSM (all) + FI	-	86.50%	80.53%	4.82	70.52%	92.24%	27.27%	11.23%	19.56	52.67%	80.10%
DSM (all) + AL + FI	0.1	86.30%	80.45%	4.89	69.92%	92.20%	27.79%	11.41%	18.56	53.65%	81.02%
DSM (all) + AL + FI	0.3	86.59%	80.38%	4.88	70.87%	92.29%	29.00%	12.08%	19.13	54.95%	81.21%
DSM (all) + AL + FI	0.5	86.46%	80.43%	4.94	70.48%	92.23%	28.14%	12.00%	18.82	55.58%	81.75%
DSM (all) + CS	-	86.47%	80.36%	4.79	71.23%	92.39%	27.27%	11.44%	19.17	54.06%	80.77%
DSM (all) + AL + CS	0.1	86.18%	80.19%	4.81	71.16%	92.32%	26.86%	11.49%	20.05	51.14%	79.21%
DSM (all) + AL + CS	0.3	86.29%	80.23%	4.75	72.28%	92.43%	28.45%	11.78%	18.61	54.13%	81.73%
DSM (all) + AL + CS	0.5	86.38%	80.17%	4.81	70.81%	92.41%	26.73%	10.84%	19.82	55.60%	81.07%
		CVUSA -> CVUSA					CVUSA -> CVACT				
DSM [36]*	-	93.29%	80.54%	5.29	47.49%	93.25%	38.11%	18.43%	15.48	32.45%	72.18%
DSM (all)	-	94.99%	84.30%	4.53	50.76%	95.01%	41.40%	20.03%	13.90	35.08%	75.82%
DSM (all) + AL	0.1	94.75%	84.47%	4.75	48.39%	94.15%	39.03%	18.32%	13.82	32.98%	74.38%
DSM (all) + AL	0.3	94.90%	84.76%	4.76	47.20%	93.67%	41.15%	20.32%	13.99	33.17%	74.01%
DSM (all) + AL	0.5	94.82%	84.87%	5.03	46.14%	93.05%	40.61%	19.50%	13.50	33.70%	75.10%
DSM (all) + FI	-	95.30%	84.91%	3.77	81.04%	96.71%	41.58%	19.44%	13.34	52.20%	79.56%
DSM (all) + AL + FI	0.1	95.32%	85.21%	3.85	81.21%	96.63%	42.97%	20.67%	12.93	52.62%	79.47%
DSM (all) + AL + FI	0.3	95.29%	84.98%	3.78	82.13%	96.77%	41.93%	20.07%	13.15	52.94%	79.77%
DSM (all) + AL + FI	0.5	95.35%	85.28%	3.84	82.15%	96.76%	42.02%	20.01%	13.30	52.17%	79.39%
DSM (all) + CS	-	95.32%	84.84%	3.73	81.80%	96.79%	42.71%	20.59%	12.77	53.83%	80.14%
DSM (all) + AL + CS	0.1	95.19%	84.93%	3.74	82.20%	96.78%	42.78%	20.34%	12.92	52.36%	79.88%
DSM (all) + AL + CS	0.3	95.27%	85.19%	3.77	82.42%	96.75%	42.37%	20.00%	13.02	54.30%	80.21%
DSM (all) + AL + CS	0.5	95.29%	85.24%	3.84	81.84%	96.74%	42.40%	20.24%	12.85	52.30%	80.05%

A.9 Best and worst example visualization

Figure 10-17 show the visualization of the best matched cases (top 5 correctly matched queries with the highest margin between the similarity scores of the top 1 and the top 2 prediction) and the worst mismatched cases (top 5 wrongly matched queries with the highest margin between the similarity scores of top 1 prediction and the correct match). Each row shows the street-view query, matched satellite image (yellow line indicates the extracted orientation, the red line indicates the ground truth), Top 5 prediction results (green line indicates the extracted orientation) with similarity scores. Note that in Figure 11, all five samples have GPS drift, the actual camera locations are not at the center of the ground truth images. Besides the third row, the other four worst samples actually find better-matched images (the top 1 images are closer to the correct location) than the ground truth images and the orientation estimations are correct.



Figure 10: Top best samples from CVACT [25] FI model with highest similarity margins.



Figure 11: Top worst samples from CVACT [25] FI model with highest similarity margins.

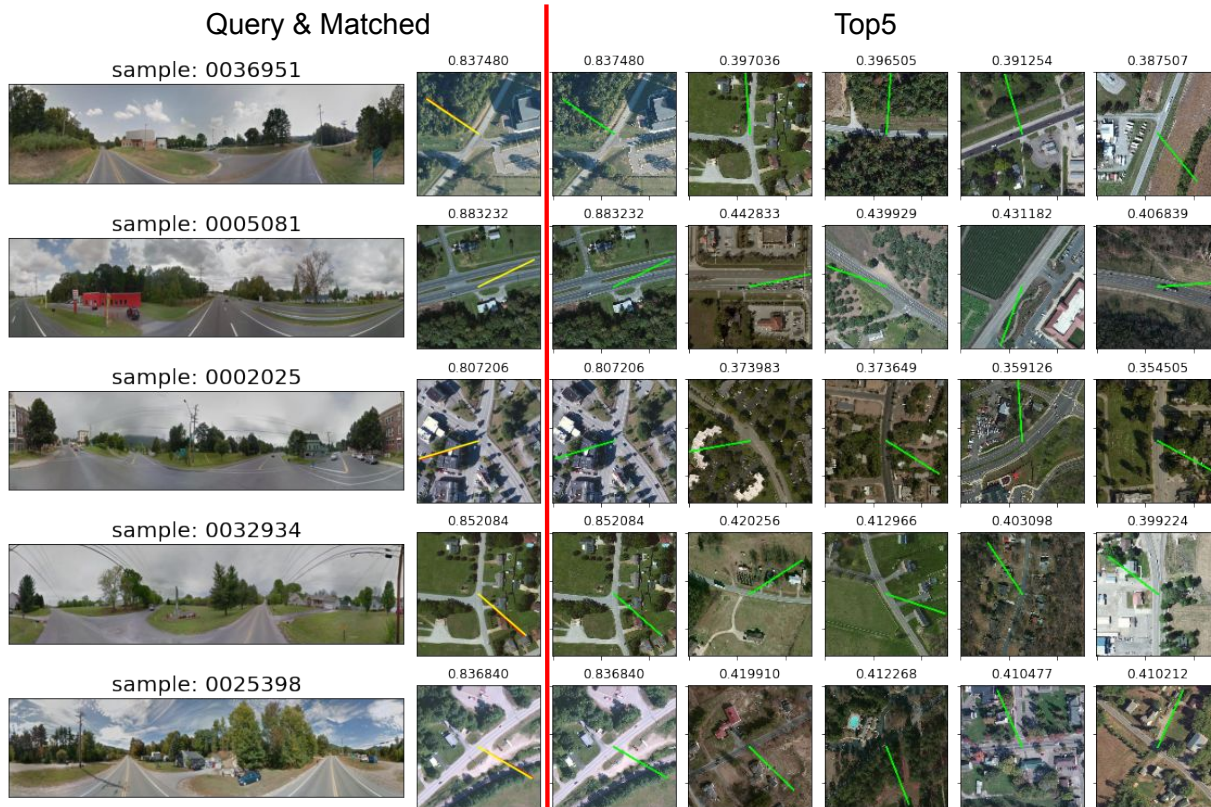


Figure 12: Top best samples from CVUSA [50] CS model with highest similarity margins.

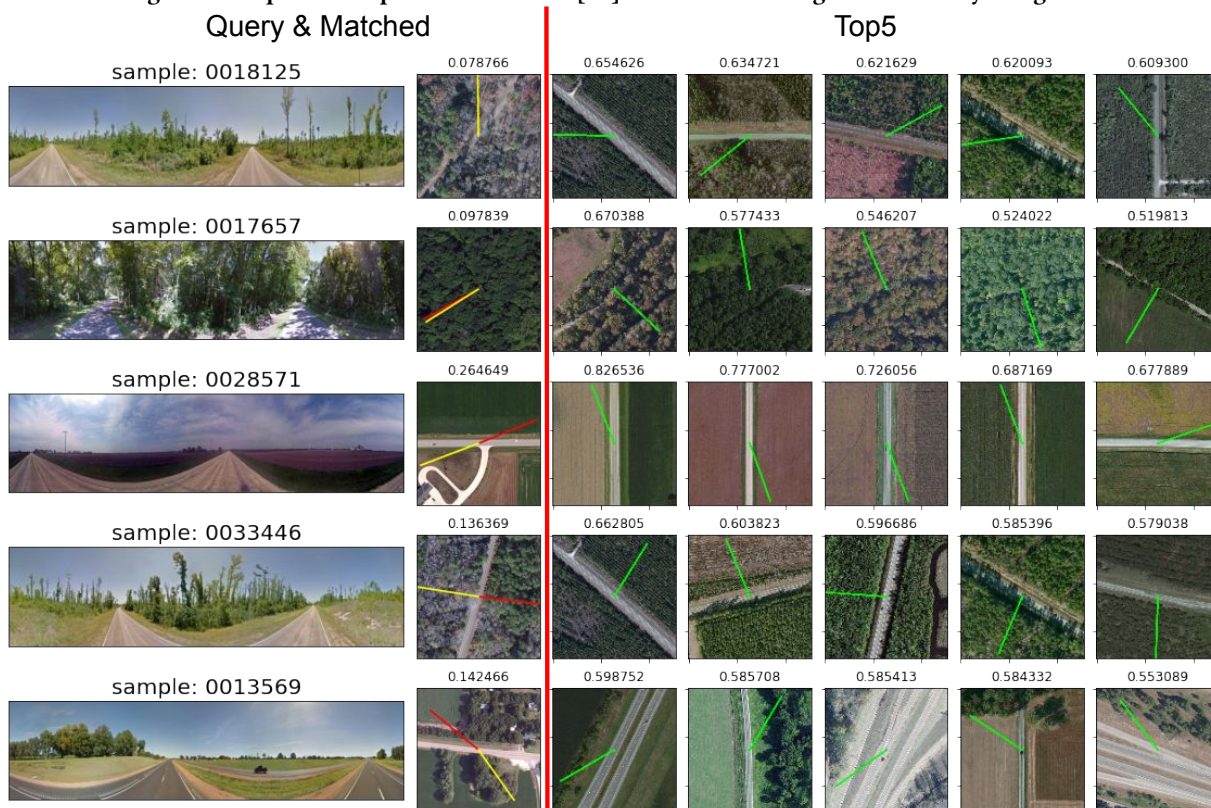


Figure 13: Top worst samples from CVUSA [50] CS model with highest similarity margins.

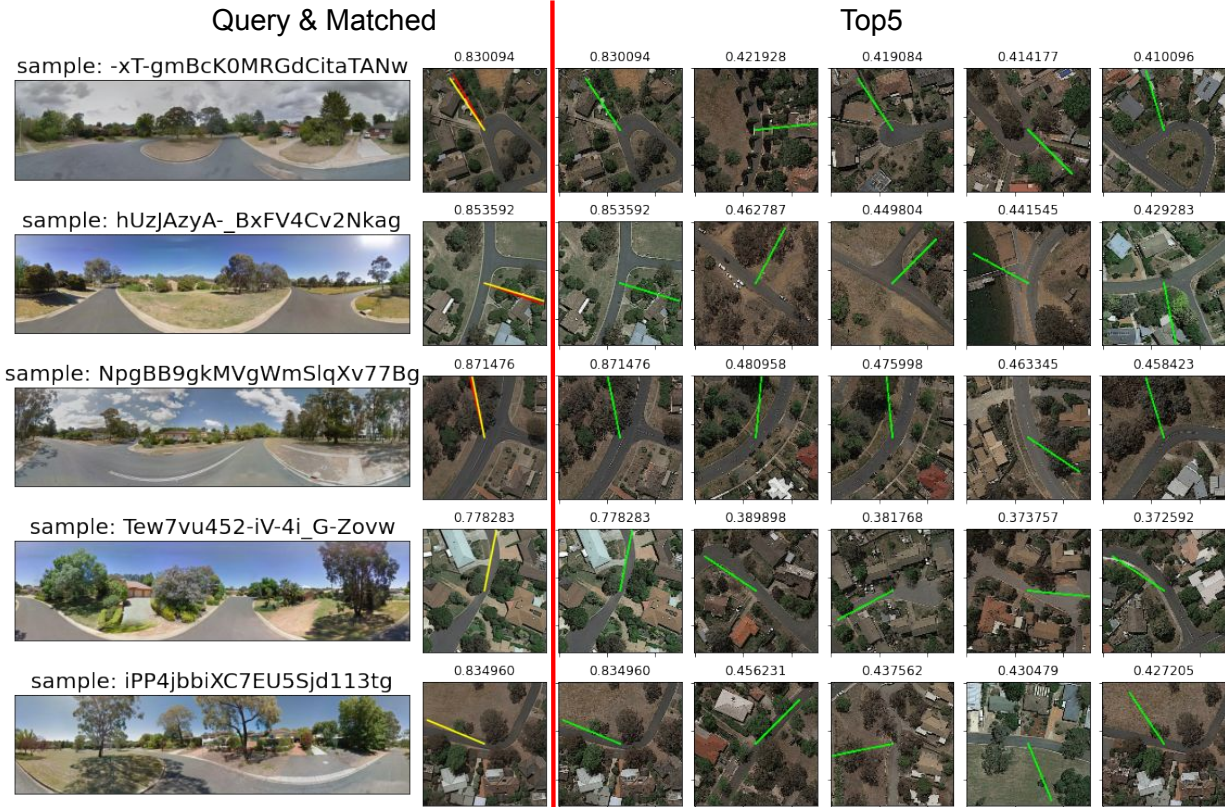


Figure 14: Top best samples from CVACT [25] DSM [36]* model with highest similarity margins.



Figure 15: Top worst samples from CVACT [25] DSM [36]* model with highest similarity margins.



Figure 16: Top best samples from CVUSA [50] DSM [36]* model with highest similarity margins.

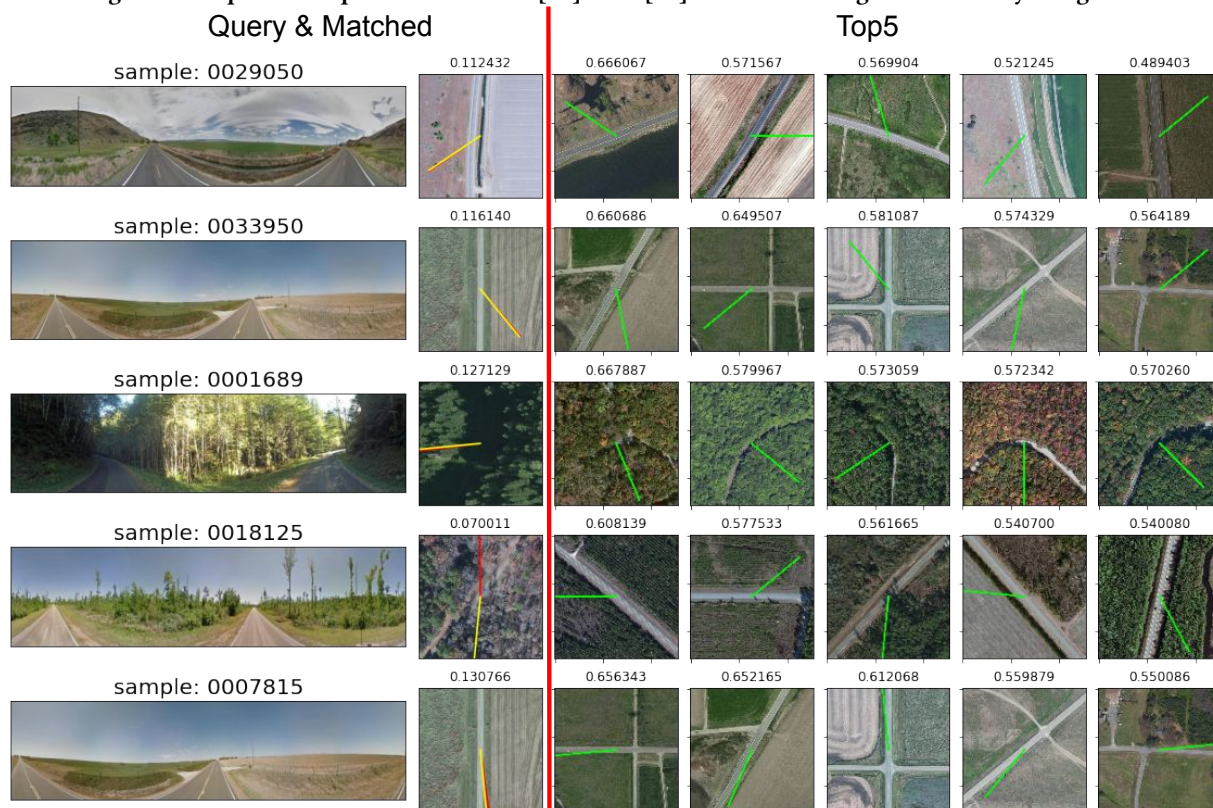


Figure 17: Top worst samples from CVUSA [50] DSM [36]* model with highest similarity margins.